Simple Dark-Field Microscopy with Nanometer Spatial Precision and Microsecond Temporal Resolution

Hiroshi Ueno,[†] So Nishikawa,[‡] Ryota Iino,[†] Kazuhito V. Tabata,[†] Shouichi Sakakihara,[†] Toshio Yanagida,[‡] and Hiroyuki Noji[†*]

[†]Institute of Scientific and Industrial Research, and [‡]Laboratories for Nanobiology, Graduate School of Frontier Biosciences, Osaka University, Osaka, Japan

ABSTRACT Molecular motors such as kinesin, myosin, and F_1-ATPase are responsible for many important cellular processes. These motor proteins exhibit nanometer-scale, stepwise movements on micro- to millisecond timescales. So far, methods developed to measure these small and fast movements with high spatial and temporal resolution require relatively complicated experimental systems. Here, we describe a simple dark-field imaging system that employs objective-type evanescent illumination to selectively illuminate a thin layer on the coverslip and thus yield images with high signal/noise ratios. Only by substituting the dichroic mirror in conventional objective-type total internal reflection fluorescence microscope with a perforated mirror, were nanometer spatial precision and microsecond temporal resolution simultaneously achieved. This system was applied to the study of the rotary mechanism of F_1-ATPase. The fluctuation of a gold nanoparticle attached to the γ-subunit during catalytic dwell and the stepping motion during torque generation were successfully visualized with 9.1-μs temporal resolution. Because of the simple optics, this system will be applicable to various biophysical studies requiring high spatial and temporal resolution in vitro and also in vivo.

INTRODUCTION

Recent years have brought remarkable progress in techniques for single-molecule detection using micro- or nanoparticles and fluorescent markers as optical probes. These techniques include differential interference contrast microscopy (1,2), laser dark-field illumination (3–5), quadrant photodiode detection (6–8), total internal reflection fluorescence microscopy (TIRFM) (9–13), fluorescence polarization imaging (14–18), and fluorescence imaging with one-nanometer accuracy (19–22). All of these methods have contributed greatly to our understanding of the mechanisms of many biological processes (23–26), especially of the chemomechanical coupling mechanism of linear molecular motors (kinesin, myosin, dynein, and nucleic acid polymerase) and rotary motors (F_1-ATPase and bacterial flagellar motor).

Linear motor proteins work by moving along cytoskeletal polymer networks or along nucleic acid chains. Myosins move along actin filaments to cause muscle contraction. Kinesins and dyneins move along microtubules to transport cellular cargo in directions opposite to each other. Nucleic acid polymerases move along nucleic acid chains, synthesizing complementary strands. Rotary motors work by making a unidirectional rotation. F_1-ATPase is the water-soluble portion of F_oF_1-ATP synthase which catalyzes ATP synthesis/hydrolysis coupled with a transmembrane proton-translocation via intersubunit-rotation (27–29). Isolated F_1-ATPase acts as a rotary motor driven by ATP hydrolysis (30). The bacterial flagellar motor is a membrane-bound macromolecular complex that swivels the flagellar filaments, propelling a cell body through liquid media. It is driven by the transmembrane flow of ions down the electrochemical potential difference across the membrane (31–33). It converts chemical (or electrochemical) energy into mechanical work. Such molecular motors have nanometer-scaled structures that catalyze reactions in the micro- to millisecond timescales (4,5,34), so one must be able to measure their movements with nanometer spatial resolution and micro- to millisecond temporal resolution for understanding fully their mechanical work and motion.

In previous studies, several researchers have succeeded in measuring the small and fast movements of molecular motors using gold nanoparticles (40–200 nm) as probes for dark-field imaging (4,5,35,36). Because the viscous friction of a gold nanoparticle is extremely low, gold labeling imposes nearly no load and can follow fast movement of molecular motors. Thus, gold nanoparticles can be used in a manner similar to a single fluorophore as a tracking probe. Furthermore, unlike fluorescent probes, gold nanoparticles do not suffer from photobleaching or blinking and can produce stronger and more stable signal intensity—and therefore, greater spatial and temporal resolution—than fluorescent probes. However, relatively large and complicated pieces of equipment are still required to realize such high spatial and temporal resolutions (4,5,35,36).

In this study, we have developed a simple dark-field imaging system that employs the perforated mirror and objective-type evanescent illumination to selectively illuminate a thin region adjacent to the glass-water interface. By merely substituting the dichroic mirror used in conventional optics with the perforated mirror, dark-field imaging with nanometer spatial precision and microsecond temporal

Submitted August 29, 2009, and accepted for publication January 5, 2010.

*Correspondence: hnoji@sanken.osaka-u.ac.jp

Editor: E. Michael Ostap.

0006-3495/10/05/2014/10 $2.00

doi: 10.1016/j.bpj.2010.01.011

resolution was realized. We employed this simple imaging system to visualize the stepping behaviors of the rotary motor F_1-ATPase. Here, we present details of our experimental system and report the results of its application to the measurement of the rotary motor protein.

MATERIALS AND METHODS

Microscope setup

Fig. 1 shows a schematic drawing of dark-field microscope systems used to visualize gold nanoparticles. We performed dark-field imaging by objective-type total internal reflection dark-field microscopy (TIRDFM) (see Fig. 1 *A*). We also constructed an objective-type vertical illumination dark-field microscopy (VIDFM) system for comparison purposes (see Fig. 1 *B*). We used a commercial microscope (IX71; Olympus, Tokyo, Japan) with a perforated mirror (PM) and a dot mirror (DM). Illumination was performed by a 532-nm diode-pumped Nd:YVO_4 laser (DPGL-2050; Suwtech, Shanghai, China), which was attenuated by neutral density filters (ND) and passed through a 10× beam expander (BE). The collimated incident laser beam was reflected by a mirror (M) and focused by a lens (L, f = 300 mm) onto the back focal plane of the objective lens (PlanApo N, 60×, numerical aperture (NA) 1.45, Olympus). The laser beam was reflected by the mirror (PM, DM) before entering the objective lens to achieve dark-field imaging. The PM and DM were manufactured by Sigma Koki (Santa Ana, CA) and in-house, respectively. Light absorbing material (Edmund Optics, Tokyo, Japan) was attached to the back side of the reflecting surface of each mirror (PM and DM) to avoid stray light from the transmitting laser light through the mirror. To produce evanescent illumination, the incident laser beam was steered to the outer edge of the objective's back aperture by tilting a mirror (M). The beam reflected at the glass-water interface was again reflected by the PM. The PM has an elliptical antireflecting surface (minor axis = 4 mm, major axis = 5.66 mm, circular window viewed from the optical axis) in its central region to transmit scattered light through this area. In contrast, the DM has an elliptical reflecting surface (minor axis = 3 mm, major axis = 4.24 mm) in its central region, and it transmits scattered light through other areas. The laser beam reflected by the DM was steered to the center of the objective's back aperture to produce vertical illumination (see Fig. 1 *B*). The illumination area was ~23 × 23 μm in both cases. The scattering image of the sample was recorded as an eight-bit AVI file with a high-speed CMOS camera (FASTCAM-1024PCI; Photron, Tokyo, Japan) at various frame rates. Effective pixel size of the detector was 88.5 nm. Image acquisition was performed by commercial software (PFV, Photron). Custom software was used to determine the position of each nanoparticle image by a previously published method (4,19,37–39).

Signal/noise ratio

The signal/noise ratio (SNR) for the gold nanoparticle spot was calculated as the difference in integrated intensities between the image that contained the single spot and that of background, divided by the noise level, as

$$SNR = (I_s - I_b)/\sqrt{\sigma_s^2 + \sigma_b^2}, \quad (1)$$

where I_s is signal intensity, I_b is background intensity, and ${\sigma_s}^2$ and ${\sigma_b}^2$ are their variances, respectively (37,40). Signal intensity of the object was measured from an area of 16 × 16 pixels (1.4 × 1.4 μm) that contained a single gold nanoparticle spot, and the adjacent background area of 16 × 16 pixels (1.4 × 1.4 μm) was measured for background intensity.

Precision measurement

Precision of position determination for our experimental system was obtained from the analysis of a gold nanoparticle fixed onto the coverslip.

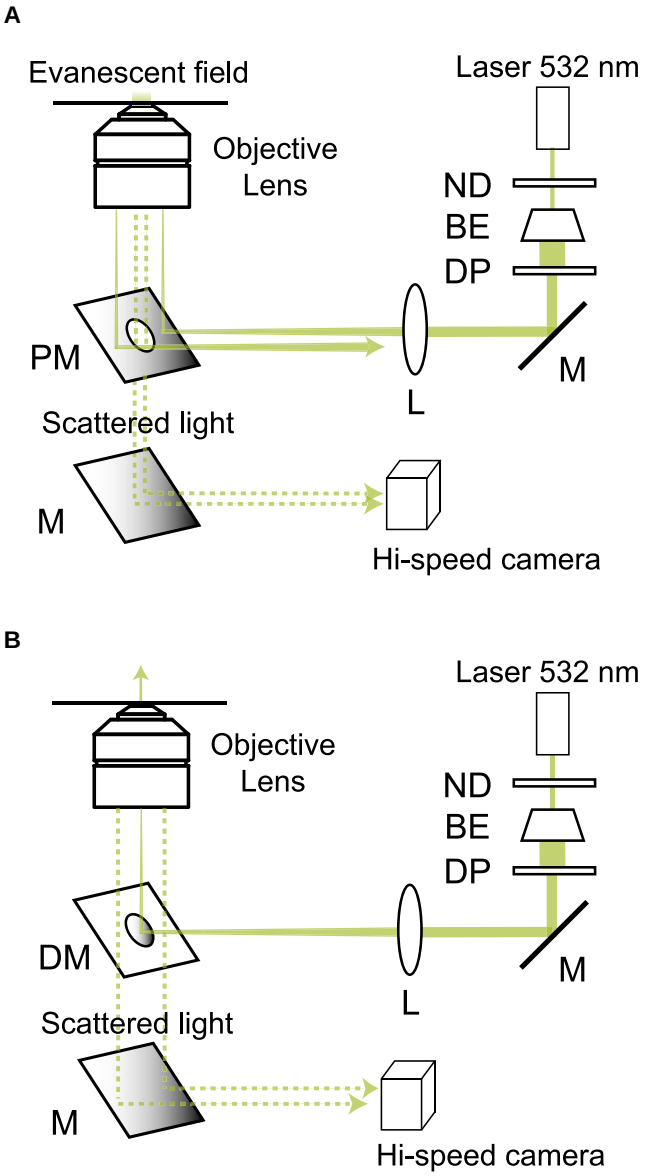

FIGURE 1 Experimental setup. (ND) neutral density filter, (BE) laser beam expander, (DP) diaphragm, (M) mirror, (L) lens, (PM) perforated mirror, and (DM) dot mirror. (*A*) Schematic drawing of objective-type TIRDFM. Incident laser beam is steered to the outer edge of objective's back aperture to produce evanescent illumination. Beam reflected at glass-water interface is again reflected by the PM. The PM has an elliptical antireflecting surface (with minor axis = 4 mm and major axis = 5.66 mm) at its central region to transmit scattered light. Light scattered by gold nanoparticle is imaged by a high-speed camera. (*B*) Schematic drawing of objective-type VIDFM. Incident laser beam is reflected by the DM. The DM has an elliptical reflecting surface (with minor axis = 3 mm and major axis = 4.24 mm) at its central region. Reflected laser beam is steered to center of the objective's back aperture to produce vertical illumination. The scattered light is transmitted through the region that is uncovered with reflecting material of the DM.

A 40-nm-diameter gold nanoparticle was fixed onto the glass surface under a high-ionic-strength solution. Diffraction-limited images were recorded at various frame rates. Center positions of each gold nanoparticle were determined by custom software using two algorithms based on a previously published method (4,19,37–39). The first method was a centroid calculation given by the expression

$$f_{x(\text{or } y)} = \sum x_i(\text{or } y_i) \times (I_i - I_t) / \sum (I_i - I_t), \quad (2)$$

where x_i (or y_i) is the coordinate of a pixel on the x (or y) axis, I_i is pixel intensity, and I_t is threshold value. The threshold was set to the maximum background intensity near the gold nanoparticle spot.

The second method was a two-dimensional (2D) Gaussian fit of the general form

$$f(x,y) = A \times \exp\left[-(x-x_0)^2/2\sigma_x^2 - (y-y_0)^2/2\sigma_y^2 \right] + B, \quad (3)$$

where x_0 and y_0 are center coordinates of the Gaussian, ${\sigma_x}^2$ and ${\sigma_y}^2$ are variances of the Gaussian, A is amplitude, and B is baseline. We fitted the 2D-Gaussian to the intensity profile using the Levenberg-Marquardt algorithm (41). Localization precision was defined as the standard deviation of center positions in a 1-s window. Finally, we plotted localization precision versus power of incident laser beam or integration time.

F_1-ATPase and gold nanoparticle preparation

The $\alpha_3\beta_3\gamma$ subcomplex of F_1-ATPase, the minimum motor complex, was used for rotation assay and will hereafter be referred to as F_1-ATPase (30). F_1-ATPase from thermophilic *Bacillus* PS3 was purified and biotinylated at cysteines of the γ-subunit, as reported previously (4,42,43). Streptavidin-coated gold nanoparticle was prepared as follows: Colloidal gold (40-nm diameter, British BioCell International, Cardiff, UK) was suspended in 10 mM potassium phosphate buffer, pH 8.0, containing 3 mg/mL Tween 20, and allowed to stand for 30 min. To generate a biotin-functionalized self-assembled monolayer on a gold surface, the gold solution (9×10^{10} particles/mL) was modified with the alkanethiol solution containing 0.4% (v/v) PEG6-COOH alkanethiol, 0.1% (v/v) PEG6-OH alkanethiol, and 0.01% (w/v) biotinylated PEG alkanethiol (SensoPath Technologies, Bozeman, MT) and allowed to stand for 48 h at 70°C. After removing unreacted alkanethiol solution, 1 mg/mL streptavidin in 10 mM potassium phosphate buffer, pH 8.0 was added. After excess streptavidin was removed by centrifugation, the pellet was resuspended in 10 mM borate buffer, pH 8.0, and stored at 4°C until use.

Rotation assay

A flow cell was constructed from a Ni^{2+}-NTA-coated cover glass and an uncoated cover glass separated by two spacers with ~50 μm thickness (29). At first, we infused buffer R (20 mM MOPS/KOH, pH 7.0, 50 mM KCl, 2 mM $MgCl_2$, 5 mg/mL BSA) into the flow cell and waited for 5 min to block nonspecific binding of the enzyme. Biotinylated F_1 (40–80 pM)—which has His-tags at the N-terminus of α- and β-subunits—in buffer R was infused. After 10 min, unbound F_1 was washed with buffer R. Then, we infused streptavidin-coated gold nanoparticle in buffer R and waited for 10 min. Unbound nanoparticle was removed with buffer R that contained the indicated concentration of ATP and an ATP-regeneration system (4,44), and observation of rotation was started at 25 ± 1°C.

RESULTS AND DISCUSSION

Objective-type TIRDFM

Fig. 1 *A* shows the schematic image of the objective-type total internal reflection dark-field microscopy (TIRDFM). Illumination was performed by a 532-nm laser whose wavelength is close to a plasmon-resonance wavelength maximum of a 40-nm gold nanoparticle (45), because the collimated laser beam can be focused to a fine spot of high power density essential for imaging with high spatio-temporal resolution and easily realize TIR-illumination compared to the collimated arc lamp. As an arc light source can also realize TIR-illumination (46), our system would also work under arc lamp illumination. The perforated mirror (PM) was placed at the position of a dichroic mirror in a conventional objective-type TIRFM system to reflect the laser beam. Then, the incident laser is reflected at the water-glass interface, forming the evanescent field on the coverslip surface. The evanescent field induces the dipoles in the specimen (small gold nanoparticle) and the oscillating dipoles within the particle leads to conversion of the nonpropagating near-field light into the conventional propagating scattered light, a part of which passes through the central window of the PM to the camera. This scattering process is known as frustrated total internal reflection, and has been used in scattering scanning near-field microscopy (47,48). For background elimination, the returning laser is again reflected by the PM not to reach the camera.

The essential modification in this system from the conventional TIRFM is merely the substitution of a dichroic mirror with the PM. Although there are several variations of TIRDFM (49,50), this system, unlike other systems, does not require an additional iris and or a dichroic mirror (or beam splitter) to avoid a loss of signal. We also constructed another type of a dark-field microscopy by placing the dot mirror (DM) instead of the PM to build an objective-type vertical illumination dark-field microscopy (VIDFM), which is similar to the laser oblique illumination (3,35) for comparison purpose. In the VIDFM, the incident laser is vertically introduced from the center of the back focal plane of the objective lens after being reflected at the DM (see Fig. 1 *B*). The scattered light from the specimen is transmitted through the region uncovered with reflecting material of the DM. We tested another type of mirror which has two elliptical reflecting surfaces located at the same distance from the optical axis for TIR-illumination. Although this is simpler than the elliptical anti-reflecting surface for PM, we did not employ this mirror because the focused image was highly distorted probably due to the asymmetric masking of parallel scattered light (data not shown).

Visualization of gold nanoparticles by objective-type TIRDFM

Gold nanoparticles of 40-nm diameter fixed onto a glass surface were visualized by TIRDFM and VIDFM. Fig. 2 *A* shows images of immobile single gold nanoparticle spots. It is obvious that TIRDFM provided a clear image with low and uniform background noise. In contrast, objective-type VIDFM showed sharp spots but relatively high and nonuniform background noise. As the dot mirror in objective-type VIDFM has a reflecting surface in the center, interference of laser light by multiple reflections in the optics and stray light caused high and nonuniform background noise, especially at the center of the image (see Fig. 2 *A, right*).

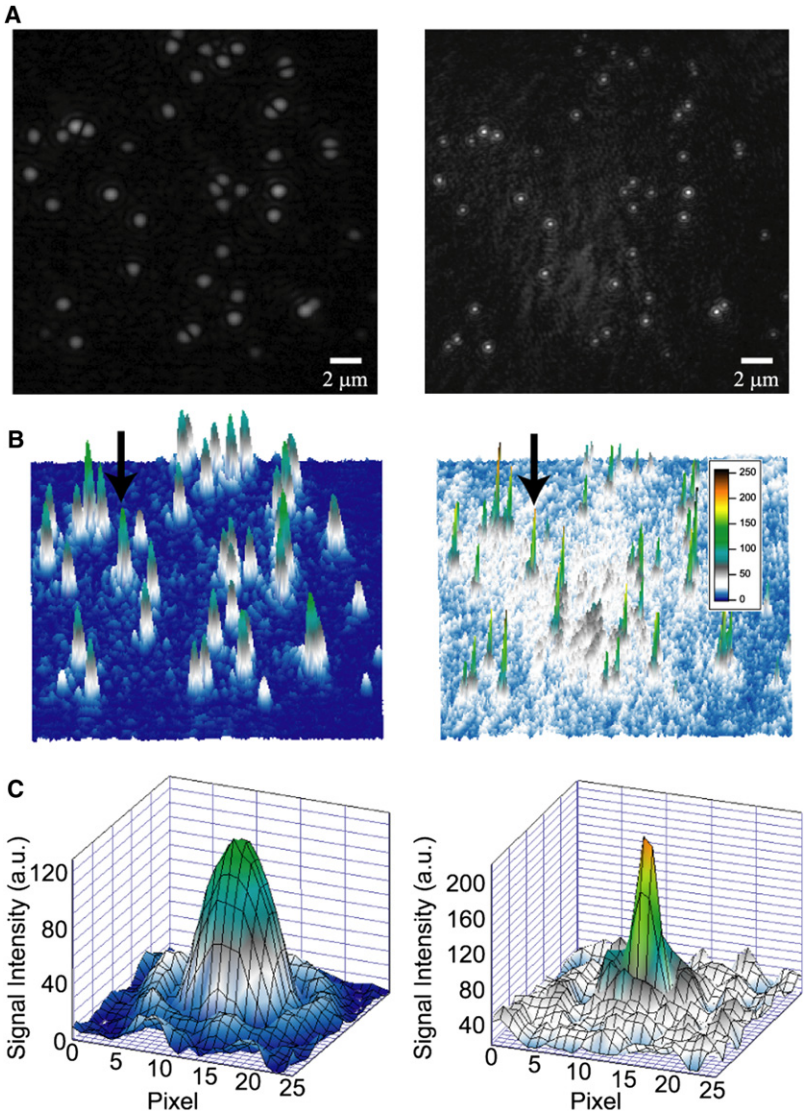

FIGURE 2 Typical images of single 40-nm gold nanoparticles fixed onto glass surface by objective-type TIRDFM (*left*) and VIDFM (*right*). Images were recorded with 0.1-ms integration time. Power of incident laser was 7.6 $\mu W/\mu m^2$, and illumination area was ~23 × 23 μm. (*A*) Raw images of 40-nm gold nanoparticles by TIRDFM (*left*) and VIDFM (*right*) on glass surface in the same visual field. Scale bar = 2 μm. (*B*) Intensity profiles of 40-nm gold nanoparticles shown in panel *A*. Apparently, TIRDFM provided better image with low and uniform background noise. VIDFM image showed high and nonuniform background noise. (*C*) Extended profile indicated by arrow in panel *B*. Pixel size = 88.5 nm. Profile was fitted by 2D-Gaussian. FWHM of PSF were 672 ± 36 and 623 ± 41 nm (n = 15), and 259 ± 48 and 212 ± 34 nm (n = 15) in the x- and y directions, for TIRDFM and VIDFM, respectively. Values are means ± SD.

Intensity profiles of the images in Fig. 2 *A* are shown in Fig. 2, *B* and *C*. A 40-nm diameter gold nanoparticle is sufficiently small compared to the wavelength of the incident laser beam to be treated as a point source. Because of diffraction, the gold nanoparticle is imaged as the Airy disk which has a 2D intensity profile referred to as the point spread function (PSF) (51). It has been shown that the PSF can be approximated well by a 2D-Gaussian (37,39). Therefore, each full width at half-maximum (FWHM) of the spots visualized by TIRDFM and VIDFM was determined by fitting with the 2D-Gaussian. Values obtained were 672 ± 36 and 623 ± 41 nm (n = 15), and 259 ± 48 and 212 ± 34 nm (n = 15) in the x and y directions, for TIRDFM and VIDFM, respectively.

Overall, the FWHM of the x direction was larger than that of the y direction. Because the FWHM of the y direction became larger than that of the x direction after rotating the camera 90° clockwise, it appeared that the difference in the FWHM between the x and y directions comes from the distortion of the shape of the transmitting surface of the PM and DM, but not from the property of the detector. The diffraction-limited FWHM, ~0.5λ/NA (51), is 183 nm at λ = 532 nm and NA = 1.45 theoretically. The FWHM of the spots by VIDFM is relatively close to the theoretical value, thus indicating that VIDFM exhibited a smaller loss in numerical aperture by the DM. In contrast, we can see that there is a large difference between the FWHM of the spots by TIRDFM and the theoretical value. This large difference was caused by the perforated mirror (PM). The PM can transmit the parallel light beam from the objective lens through the centrally located antireflecting window, but the diameter of the parallel light beam, 2 × NA × f = 8.7 mm (NA = 1.45, f = 3 mm), is larger than that of the antireflecting surface (4 mm). Thus, our design caused the rejection of parallel light collected by the high NA region of the objective lens, which resulted in the decrease of effective

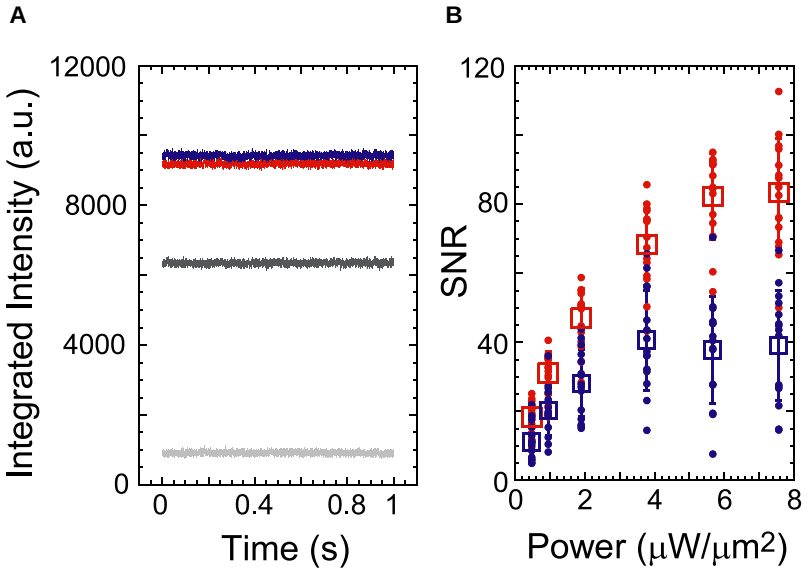

FIGURE 3 SNR of images by objective-type TIRDFM and VIDFM with integration time of 0.1 ms. (*A*) Typical scattering intensities of 40-nm gold nanoparticle spot detected by TIRDFM (*red trace*) and VIDFM (*blue trace*) and background intensities adjacent to each object (TIRDFM, *light gray trace*; VIDFM, *dark gray trace*) were plotted as function of time at laser power of 7.6 $\mu W/\mu m^2$. (*B*) SNR plotted as function of incident laser power. (*Red circles* and *squares*) SNR for individual gold nanoparticles, and SNR averaged over different particles by TIRDFM, respectively. (*Blue circles* and *squares*) SNR for individual gold nanoparticles, and SNR averaged over different particles by VIDFM, respectively.

NA of this system. Actually, the effective NA was determined to be ~0.4 from the experimental value of the FWHM.

Although FWHM increased due to the low NA, it is possible to determine the position of a single point source with nanometer precision (1,19,39). We will describe the precision of position determination for our experimental system in the following paragraph.

SNR

We determined SNR at various power densities of the incident laser beam with a temporal resolution of 0.1 ms. To determine SNR, we measured time traces of scattering intensities of gold nanoparticle spots and also background intensities adjacent to the object. Fig. 3 *A* shows typical time traces of signal intensities from a single gold nanoparticle spot and background intensities detected by TIRDFM (signal: *red trace,* background: *light gray trace*) or VIDFM (signal: *blue trace,* background: *dark gray trace*). At laser power of 7.6 $\mu W/\mu m^2$, the signal intensity from TIRDFM and VIDFM were 9194 ± 53 arbitrary units (a.u.) and 9423 ± 58 a.u., respectively. In spite of lower effective NA, the TIRDFM gave comparative signal intensity to that of VIDFM. This is due to the surface enhancement of the evanescent wave's intensity, which can be severalfold more intense than the incident laser beam under TIR illumination (10,13). A large difference was the background intensity. Whereas the background level of the TIRDFM was only 908 ± 46 a.u., VIDFM gave much higher background, 6347 ± 52 a.u. at 7.6 $\mu W/\mu m^2$. This is because the TIRDFM limits the illumination volume to the glass surface and reduces the stray light, compared to VIDFM. Resultantly, SNR calculated with Eq. 1 was 1.5–2.1 times higher for TIRDFM than for VIDFM under all power conditions (see Fig. 3 *B*). SNR increased with higher illumination power. This was explained by the increase in the net signal intensity in Eq. 1 ($I_s - I_b$), because the noise term in Eq. 1 increased only slightly with increasing illumination power. For example, the noise term at maximum laser power of 7.6 $\mu W/\mu m^2$ only increased 1.2–1.4-fold compared to that at minimum laser power of 0.5 $\mu W/\mu m^2$, although the net signal intensity increased five-to-sixfold in both systems. At an illumination power >5.7 $\mu W/\mu m^2$, SNR became saturated because the signal intensity tended to saturate at these conditions although all pixel values of image were below the 8-bit maximum value of 255.

Thus, TIRDFM has a significant SNR advantage for imaging compared to VIDFM. Therefore, TIRDFM can reduce radiation pressure and sample damage by the incident laser beam compared to non-TIR microscopy.

Experimental determination of localization precision

We determined localization precision of our system by measuring the position of immobile gold nanoparticles with 0.1-ms temporal resolution at several levels of incident laser power (see Fig. 4 *A*). When localization precision was determined by a centroid calculation, it reached, at laser power of 7.6 $\mu W/\mu m^2$, 1.5 ± 0.5 and 1.7 ± 0.4 nm for TIRDFM, and 1.5 ± 0.5 and 1.3 ± 0.4 nm for VIDFM in the *x* and *y* directions, respectively (see Fig. 4 *A*). The two dark-field imaging systems showed essentially the same precision value although the precision of TIRDFM was lower than that of VIDFM only at low laser power. When the localization precision was determined by 2D-Gaussian fit, the precision was improved as reported (37), but the extent of the improvement was very small (see Fig. S1 in the Supporting Material): 1.2 ± 0.3 and 1.6 ± 0.4 nm for TIRDFM, and 1.4 ± 0.6 and 2.2 ± 0.7 nm for VIDFM in the *x* and *y* directions,

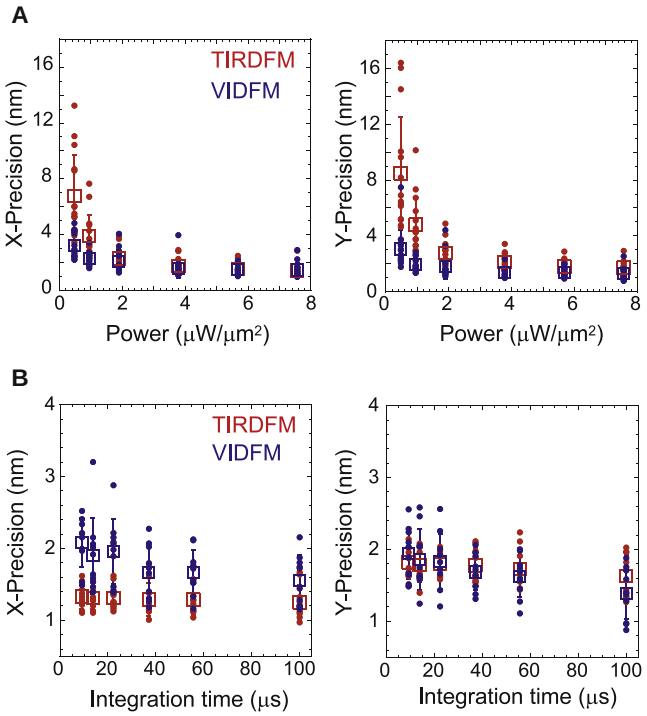

FIGURE 4 Localization precision of experimental system in *x*- (*left*) and *y* directions (*right*). (*A*) Images were acquired by TIRDFM (*red*) and VIDFM (*blue*) with integration time of 0.1 ms at several levels of incident laser power, and center positions of gold nanoparticles were determined by centroid calculation. Precisions were calculated from standard deviations of the centroid position of a gold nanoparticle in a 1-s window and plotted as function of laser power. (*B*) Localization precision as function of integration time. Images were acquired at laser power of 7.6 $\mu W/\mu m^2$ with several integration times of the camera, and center positions of gold nanoparticles were determined by centroid calculation. Precisions were plotted as function of integration time of detector. (*Red circles* and *squares*) Precisions for individual measurements, and precisions averaged over different measurements by TIRDFM, respectively. (*Blue circles* and *squares*) Precisions for individual measurements, and precisions averaged over different measurements by VIDFM, respectively. Even at 9.1-μs temporal resolution, centroid localization with nanometer precision was achieved.

respectively, at a maximum. When illumination laser power was >3.8 $\mu W/\mu m^2$, the precision of VIDFM determined by the 2D-Gaussian fit got rather worse. This is because the image acquired by VIDFM could not be fitted well by a 2D-Gaussian due to high and nonuniform background noise at high laser power. Considering the relatively small extent of the improvement by 2D-Gaussian fit and that 2D-Gaussian analysis demands relatively a long time for calculation, e.g., it is necessary to analyze 109,500 frames to obtain the information from the 1-s data recorded at 9.1-μs temporal resolution, the particle position was determined by the centroid calculation in the following parts. We also measured the dependence of precision on NA by changing the size of an antireflecting surface (see Fig. S2 in the Supporting Material). The precision was significantly improved at the ~0.4 NA (obtained from the minor axis of 4 mm), and almost saturated at this NA. At higher NA, the precision was slightly improved, and was finest when the minor axis was 6 mm, though the optical alignment became more severe. In this work, we adopted the perforated mirror, which has the minor axis of 4 mm that can easily realize 1–2-nm precision.

Next, we measured the localization precision at several integration times of the camera (see Fig. 4 *B*). As integration time decreased (in other words, as temporal resolution became higher), localization precision tended to decrease. However, our system has ultimately achieved 1–2 nm precision even with 9.1-μs temporal resolution (see Fig. 4 *B*): 1.3 ± 0.2 and 1.8 ± 0.2 nm for TIRDFM, and 2.1 ± 0.4 and 1.9 ± 0.4 nm for VIDFM in the *x* and *y* directions, respectively. There was no essential difference in the precision between these imaging systems.

To examine the effect of read-out noise on the precision, the original image sequence recorded with 9.1-μs integration time was subjected to a moving average (window size = 91 μs), and the precision was determined. As a result, the precision was improved to be 0.9 ± 0.1 and 0.9 ± 0.2 nm in the *x* and *y* directions, respectively, which are better than those determined from the image recorded with 0.1-ms integration time. This indicates that the read-out noise for each frame is a part of the causes of low dependence of the precision on the integration time.

Compared with previous dark-field imaging with the 5–6 nm precision at 0.32-ms temporal resolution (5), our systems made drastic improvement. In our system, maximum temporal resolution is limited by the selectable maximum recording rate of the high-speed camera used here, not by signal intensity. Therefore, if a high-speed camera with higher recording rate could be made available, maximum temporal resolution could be improved. Moreover, if a higher signal could be obtained by using a larger probe than the one we used in our study, it would also be possible to achieve superior spatial and temporal resolution.

Thus, the two lines of experiments on the localization precision showed the TIRDFM has the same precision at ~1–2 nm as VIDFM. The higher SNR would compensate the broader FWHM to achieve the high precision in the TIRDFM. Especially because the TIRDFM has advantages of TIR-illumination and free space above the sample chamber, this method is broadly applicable in various studies (as discussed in detail later). It should be noted that on the whole, precision in the *x* direction tends to be higher than that in the *y* direction. We defined the *x* direction in an observation plane to correspond with the horizontal signal line of the camera. This trend persisted even after rotating the camera 90° clockwise (data not shown). Therefore, the reason for this trend is most likely the intrinsic properties of the camera used in our study.

Application to rotary motor F_1-ATPase

To evaluate the usefulness of our system for the study of molecular motors, we observed the rotation of F_1-ATPase

at 9.1-μs temporal resolution, using a 40-nm gold particle as the above-mentioned measurements under the TIRDFM. It has been reported that the rotary motor F_1-ATPase generally rotates by repeating four stages, as follows: ATP-waiting pause (dwell); rapid 80° substep rotation upon ATP binding; catalytic dwell in which ATP cleavage and phosphate release occur; and rapid 40° substep rotation, triggered by release of phosphate (4,44,52,53). Previous studies using high-speed imaging with up to 0.125-ms temporal resolution revealed that catalytic dwell is ~2 ms at 23°C, and that two catalytic reactions (ATP cleavage and phosphate release) of ~1 ms occur in the catalytic dwell (4,44). Our system should be able to visualize these short events with higher resolution. We analyzed the rotation of F_1-ATPase at 2 mM ATP where catalytic dwells (~2 ms) determine the turnover rate of ATP hydrolysis coupled with rotation (4), and they should be detected with our system. Fig. 5 *A* shows the time course of rotation of F_1-ATPase at 2 mM ATP, as detected by TIRDFM. Indeed, F_1-ATPase showed stepwise rotation (see Fig. 5 *A*) with discrete 120° steps, as expected (see Fig. 5 *B*). The histogram of the dwell time showed a peak, and it was fitted with the sum of two exponential components, providing two time constants, 1.3 ± 0.1 ms and 0.3 ± 0.04 ms (see Fig. 5 *C*). These values are roughly similar to those of the previous study (1.64 ms and 0.71 ms), thus indicating that the observed pauses are the catalytic dwells (4). In our previous study at low temperatures, a highly temperature-sensitive (TS) reaction step of F_1-ATPase was found at the same angle for ATP binding and ADP release (54,55). The rate of the TS reaction at 24°C was estimated to be 6.6×10^2 s^{-1} (time constant = 1.5 ms) from the Q_{10} factor (54). However, here, we could not detect an obvious pause of the TS reaction. This is probably because the TS reaction is significantly fast under the condition of this study. Our study shows that the TS reaction is strongly dependent on the load of the probe attached to the γ-subunit, and the rate constant estimated using the small probe (~40 nm) is higher than the previously estimated one using the large probe (~200 nm) (R. Watanabe, unpublished data). From the angular fluctuation during the catalytic dwell (see Fig. 5 *B*), we determined angular resolution and stiffness of the whole system, including linker to glass surface (His-tag), F_1-ATPase itself, linker to gold nanoparticle (streptavidin), and gold nanoparticle during catalytic dwell. Standard deviation was calculated to be ~9°. Stiffness of the whole system was determined from the equipartition theorem. Because the fluctuation of a gold nanoparticle in the dwell position is in thermal equilibrium, the Boltzmann equipartition theorem states that average potential energy is equal to elastic energy, as

$$1/2k_BT = 1/2\kappa\sigma^2, \quad (4)$$

where k_B is Boltzmann's constant, T is absolute temperature, κ is torsional stiffness of the system, and σ is angular standard deviation of the gold nanoparticle from its equilibrium position. As a result, stiffness was calculated to be ~166 pN·nm. However, standard deviation determined from the position of the gold nanoparticle contains an intrinsic error from the noise component of the detection. Standard deviation of the x, y coordinates from that intrinsic error was previously determined as localization precision from measurement of the immobile gold nanoparticle (1–2 nm in Fig. 4 and Fig. S1). Therefore, given the rotation radius to be ~20 nm (see Fig. 5. *A*, *inset*), angular standard deviation was roughly calculated with the inverse tangent function to be ~3–6°. Considering this intrinsic standard deviation and the law of error propagation, actual standard deviation and stiffness were determined to be ~7–8° and ~210–275 pN·nm, respectively. This latter value is much

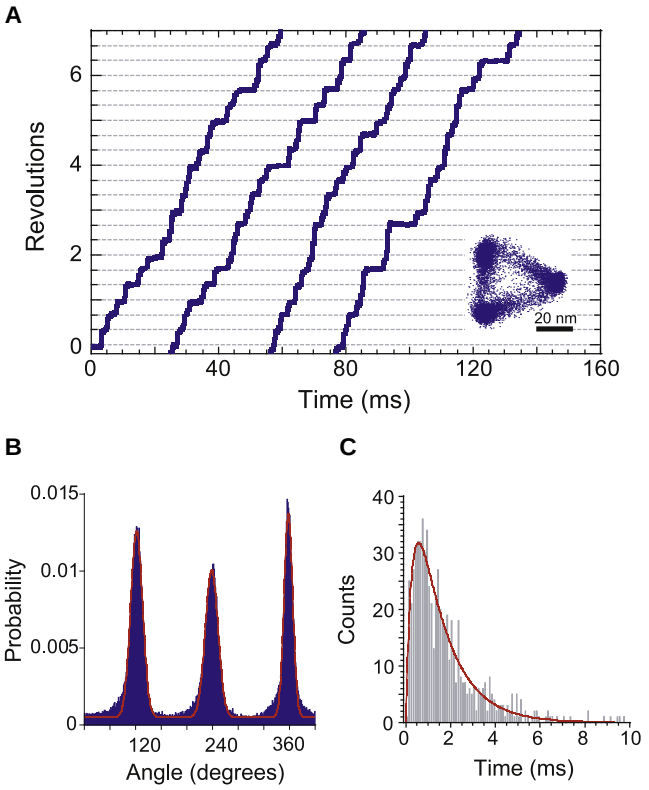

FIGURE 5 Stepwise rotation of F_1-ATPase with 9.1-μs temporal resolution. Images of 40-nm gold nanoparticle were acquired by TIRDFM and recorded at 9.1-μs temporal resolution. (*A*) Typical time courses of rotation at 2 mM ATP. (*Inset*) An *x*,*y* plot of the centroid of a gold nanoparticle. The rotation radius of a single bead up to ~26 nm $= \sqrt{(20+5+3)^2-10^2}$ is possible for the height of F_1 of ~10 nm and the linker lengths of ~5 nm for streptavidin (4) and ~3 nm for a self-assembled monolayer on a gold surface (62). (*B*) Histogram of angular position of centroid. Angular positions of pauses were determined by fitting data with Gaussian curves (*red line*) to be 121.7 ± 9.3°, 238.8 ± 9.9°, and 358.4 ± 6.7°. In this work, the angle was taken as positive for the counterclockwise direction. F_1-ATPase rotated with discrete 120° steps. (*C*) Histogram of dwell times of rotation at 2 mM ATP. (*Red line*) Fit with two rate constants: constant × [exp($-k_1$t) − exp($-k_2$t)], $k_1 = 0.75 \pm 0.05$ ms^{-1} (time constant, $\tau_1 = 1.34 \pm 0.10$ ms), and $k_1 = 3.40 \pm 0.42$ ms^{-1} (time constant, $\tau_2 = 0.29 \pm 0.04$ ms). Values are means ± SD. Total counts of dwells are 662. Bin width is 0.1 ms.

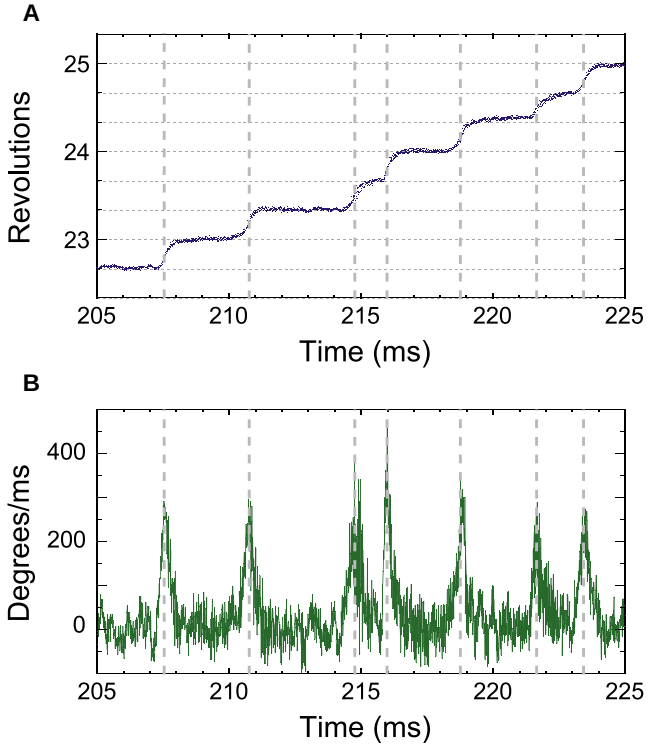

FIGURE 6 Step motion between catalytic dwells of F_1-ATPase. Expanded time courses of rotation at 2 mM ATP (*A*) and angular velocity (*B*) were plotted. Angular velocity was determined by 20-frame (0.18 ms) averaging of time derivative of accumulated rotation angle. Temporal resolution was 9.1 μs. Shaded-dashed line shows time when angular velocity became fastest. Angular velocity was not constant during 120° step between catalytic dwells.

higher than the reported value during ATP binding dwell (30 pN·nm) and the locked state under the ADP saturating condition (66 pN·nm) (56), although the group that made the calculations used F_1-ATPase from another species and larger probes. This finding implies that intrinsic stiffness of F_1-ATPase would be much higher than reported before.

Next, we focused on the step motion of F_1-ATPase between catalytic dwells. Fig. 6 shows the expanded time courses of the rotation and the angular velocity. The 120° step between catalytic dwells completed on a submillisecond timescale, which was comparable to that of previous study (~0.25 ms) (4). In the previous study, because of insufficient temporal resolution (0.125 ms), the step motion was not examined in detail. In this study, the TIRDFM enabled us to follow the step motion with much faster time resolution, 9.1 μs. Then, we found that angular velocity was not constant during the mechanical 120° step between catalytic dwells (see Fig. 6, *A* and *B*). In a typical step, F_1 showed a transient leap and the slow deceleration with the relaxation time of 0.1–0.5 ms. There are several explanations for this phenomenon:

1. Torsional stiffness of the whole system including linkers and F_1-ATPase itself causes a change in angular velocity. From autocorrelation analysis of the fluctuation of a gold nanoparticle in the dwell position, we estimated relaxation time to be approximately submilliseconds, which may, at least partly, explain this phenomenon.
2. The 120° step is further split into multiple substeps that have a short unresolved dwell time close to the response time of the probe, which causes a change in angular velocity (but this cannot be explained by a short unresolved ATP binding dwell, because ATP binding dwell occurs at an angle of forward 40° from the catalytic dwell).
3. Rotational potential is not a simple linear downhill function with constant slope, which causes angular dependences of angular velocity and torque (see Fig. S2 in the Supporting Material). Until now, it has been reported that kinesin showed a similar step motion (3,35,57), and Junge et al. (58) suggested angular dependence of the torque at F_o during ATP hydrolysis by F_1-ATPase. Further studies are needed to conclude which of these explanations is correct and to enable us to fully understand the step motion of F_1-ATPase.

SUMMARY AND CONCLUSIONS

In this study, we have developed a simple dark-field imaging system using objective-type evanescent illumination. To acquire dark-field images, the perforated mirror was applied to a conventional inverted microscope. Only by replacing the dichroic mirror in conventional objective-type TIRFM optics with the perforated mirror, were we able to acquire high-SNR images and to realize detection with nanometer localization precision and microsecond temporal resolution simultaneously.

Previously, several researchers have accomplished the detection with nanometer spatial resolution and micro-to-millisecond temporal resolution by employing a dark-field imaging method (3–5,35,36,59). However, to date, relatively complicated and large pieces of equipment have been required to realize dark-field imaging with high spatial and temporal resolution (e.g., quadrant photodiode, dark-field condenser, etc.). For this reason, use of these imaging systems has been limited to some highly skilled researchers and a specific field.

In contrast, our experimental system is simple and requires no complicated or large apparatus, and simultaneous measurement of multiple objects with high spatial and temporal resolution can be achieved easily by using a high-speed camera. Objective-type evanescent illumination used in our system provides an optical sectioning effect which is useful for visualizing events on the surface of living cells (60,61) because that can reduce the background signal even in the presence of scattering objects in solution. In addition, simultaneous observation of fluorescence and dark-field images is also easily achievable by employing filters to select fluorescence before the detector. Furthermore, our system

has free space above the sample chamber, and thus it will be applicable in various studies with configurations that require space above the sample in vitro and also in living cells (e.g., magnetic tweezers, micro-manipulators, cell culture systems, etc.).

We employed our experimental system to visualize rotation of F_1-ATPase. We succeeded in observing the rotation of F_1-ATPase with 9.1-μs temporal resolution and detected clear 120° steps and short catalytic dwells on micro-to-millisecond timescales. Because of limited temporal resolution, previous studies were unable to follow these steps in detail (4). Here, on the other hand, we could follow fast 120° steps with microsecond temporal and nanometer spatial precision, and we found that angular velocity was not constant during the 120° steps between catalytic dwells. Further detailed study will provide greater insight into this phenomenon. The simple dark-field imaging system described in this article has a great advantage in performance compared to that of previous studies, as well as the potential for application to various biophysical studies, including single molecule experiments.

SUPPORTING MATERIAL

Three figures are available at http://www.biophysj.org/biophysj/supplemental/S0006-3495(10)00138-4.

REFERENCES

1. Gelles, J., B. J. Schnapp, and M. P. Sheetz. 1988. Tracking kinesin-driven movements with nanometer-scale precision. *Nature*. 331: 450–453.
2. Kaseda, K., I. Crevel, …, R. A. Cross. 2008. Single-headed mode of kinesin-5. *EMBO Rep*. 9:761–765.
3. Nishiyama, M., E. Muto, …, H. Higuchi. 2001. Substeps within the 8-nm step of the ATPase cycle of single kinesin molecules. *Nat. Cell Biol*. 3:425–428.
4. Yasuda, R., H. Noji, …, H. Itoh. 2001. Resolution of distinct rotational substeps by submillisecond kinetic analysis of F_1-ATPase. *Nature*. 410:898–904.
5. Dunn, A. R., and J. A. Spudich. 2007. Dynamics of the unbound head during myosin V processive translocation. *Nat. Struct. Mol. Biol*. 14:246–248.
6. Finer, J. T., R. M. Simmons, and J. A. Spudich. 1994. Single myosin molecule mechanics: picoNewton forces and nanometer steps. *Nature*. 368:113–119.
7. Komori, T., S. Nishikawa, …, T. Yanagida. 2009. Simultaneous measurement of nucleotide occupancy and mechanical displacement in Myosin-v, a processive molecular motor. *Biophys. J*. 96:L4–L6.
8. Molloy, J. E., J. E. Burns, …, D. C. White. 1995. Movement and force produced by a single myosin head. *Nature*. 378:209–212.
9. Funatsu, T., Y. Harada, …, T. Yanagida. 1995. Imaging of single fluorescent molecules and individual ATP turnovers by single myosin molecules in aqueous solution. *Nature*. 374:555–559.
10. Tokunaga, M., K. Kitamura, …, T. Yanagida. 1997. Single molecule imaging of fluorophores and enzymatic reactions achieved by objective-type total internal reflection fluorescence microscopy. *Biochem. Biophys. Res. Commun*. 235:47–53.
11. Sako, Y., S. Minoghchi, and T. Yanagida. 2000. Single-molecule imaging of EGFR signaling on the surface of living cells. *Nat. Cell Biol*. 2:168–172.
12. Iino, R., I. Koyama, and A. Kusumi. 2001. Single molecule imaging of green fluorescent proteins in living cells: E-cadherin forms oligomers on the free cell surface. *Biophys. J*. 80:2667–2677.
13. Axelrod, D. 1989. Total internal reflection fluorescence microscopy. *Methods Cell Biol*. 30:245–270.
14. Forkey, J. N., M. E. Quinlan, …, Y. E. Goldman. 2003. Three-dimensional structural dynamics of myosin V by single-molecule fluorescence polarization. *Nature*. 422:399–404.
15. Nishizaka, T., K. Oiwa, …, K. Kinosita, Jr. 2004. Chemomechanical coupling in F_1-ATPase revealed by simultaneous observation of nucleotide kinetics and rotation. *Nat. Struct. Mol. Biol*. 11:142–148.
16. Masaike, T., F. Koyama-Horibe, …, T. Nishizaka. 2008. Cooperative three-step motions in catalytic subunits of F_1-ATPase correlate with 80 degrees and 40 degrees substep rotations. *Nat. Struct. Mol. Biol*. 15:1326–1333.
17. Syed, S., G. E. Snyder, …, Y. E. Goldman. 2006. Adaptability of myosin V studied by simultaneous detection of position and orientation. *EMBO J*. 25:1795–1803.
18. Ha, T., T. Enderle, …, S. Weiss. 1996. Single molecule dynamics studied by polarization modulation. *Phys. Rev. Lett*. 77:3979–3982.
19. Yildiz, A., J. N. Forkey, …, P. R. Selvin. 2003. Myosin V walks hand-over-hand: single fluorophore imaging with 1.5-nm localization. *Science*. 300:2061–2065.
20. Yildiz, A., M. Tomishige, …, P. R. Selvin. 2004. Kinesin walks hand-over-hand. *Science*. 303:676–678.
21. Kural, C., H. Kim, …, P. R. Selvin. 2005. Kinesin and dynein move a peroxisome in vivo: a tug-of-war or coordinated movement? *Science*. 308:1469–1472.
22. Churchman, L. S., Z. Okten, …, J. A. Spudich. 2005. Single molecule high-resolution colocalization of Cy3 and Cy5 attached to macromolecules measures intramolecular distances through time. *Proc. Natl. Acad. Sci. USA*. 102:1419–1423.
23. Toprak, E., and P. R. Selvin. 2007. New fluorescent tools for watching nanometer-scale conformational changes of single molecules. *Annu. Rev. Biophys. Biomol. Struct*. 36:349–369.
24. Peters, R. 2007. Single-molecule fluorescence analysis of cellular nanomachinery components. *Annu. Rev. Biophys. Biomol. Struct*. 36: 371–394.
25. Selvin, P. R., and T. Ha. 2007. Single Molecule Techniques: A Laboratory Manual. Cold Spring Harbor Laboratory Press, Cold Spring Harbor, NY.
26. Greenleaf, W. J., M. T. Woodside, and S. M. Block. 2007. High-resolution, single-molecule measurements of biomolecular motion. *Annu. Rev. Biophys. Biomol. Struct*. 36:171–190.
27. Boyer, P. D. 1997. The ATP synthase—a splendid molecular machine. *Annu. Rev. Biochem*. 66:717–749.
28. Yoshida, M., E. Muneyuki, and T. Hisabori. 2001. ATP synthase—a marvelous rotary engine of the cell. *Nat. Rev. Mol. Cell Biol*. 2:669–677.
29. Ueno, H., T. Suzuki, …, M. Yoshida. 2005. ATP-driven stepwise rotation of FoF1-ATP synthase. *Proc. Natl. Acad. Sci. USA*. 102:1333–1338.
30. Noji, H., R. Yasuda, …, K. Kinosita, Jr. 1997. Direct observation of the rotation of F1-ATPase. *Nature*. 386:299–302.
31. Sowa, Y., and R. M. Berry. 2008. Bacterial flagellar motor. *Q. Rev. Biophys*. 41:103–132.
32. Minamino, T., K. Imada, and K. Namba. 2008. Molecular motors of the bacterial flagella. *Curr. Opin. Struct. Biol*. 18:693–701.
33. Berg, H. C. 2003. The rotary motor of bacterial flagella. *Annu. Rev. Biochem*. 72:19–54.
34. Woehlke, G., and M. Schliwa. 2000. Walking on two heads: the many talents of kinesin. *Nat. Rev. Mol. Cell Biol*. 1:50–58.
35. Nan, X., P. A. Sims, and X. S. Xie. 2008. Organelle tracking in a living cell with microsecond time resolution and nanometer spatial precision. *ChemPhysChem*. 9:707–712.

36. Spetzler, D., J. York, …, W. D. Frasch. 2008. Microsecond resolution of enzymatic conformational changes using dark-field microscopy. *Methods*. 10.1016/j.ymeth.2008.05.004.
37. Cheezum, M. K., W. F. Walker, and W. H. Guilford. 2001. Quantitative comparison of algorithms for tracking single fluorescent particles. *Biophys. J*. 81:2378–2388.
38. Thompson, R. E., D. R. Larson, and W. W. Webb. 2002. Precise nanometer localization analysis for individual fluorescent probes. *Biophys. J*. 82:2775–2783.
39. Kubitscheck, U., O. Kückmann, …, R. Peters. 2000. Imaging and tracking of single GFP molecules in solution. *Biophys. J*. 78: 2170–2179.
40. Koyama-Honda, I., K. Ritchie, …, A. Kusumi. 2005. Fluorescence imaging for monitoring the colocalization of two single molecules in living cells. *Biophys. J*. 88:2126–2136.
41. Press, W. H., S. A. Teukolsky, …, B. P. Flannery. 2007. Numerical recipes. *In* The Art of Scientific Computing., 3rd Ed.. Cambridge University Press, New York.
42. Noji, H., D. Bald, …, K. Kinosita, Jr. 2001. Purine but not pyrimidine nucleotides support rotation of F_1-ATPase. *J. Biol. Chem*. 276: 25480–25486.
43. Rondelez, Y., G. Tresset, …, H. Noji. 2005. Highly coupled ATP synthesis by F_1-ATPase single molecules. *Nature*. 433:773–777.
44. Adachi, K., K. Oiwa, …, K. Kinosita, Jr. 2007. Coupling of rotation and catalysis in F_1-ATPase revealed by single-molecule imaging and manipulation. *Cell*. 130:309–321.
45. Jain, P. K., K. S. Lee, …, M. A. El-Sayed. 2006. Calculated absorption and scattering properties of gold nanoparticles of different size, shape, and composition: applications in biological imaging and biomedicine. *J. Phys. Chem. B*. 110:7238–7248.
46. Axelrod, D. 2001. Total internal reflection fluorescence microscopy in cell biology. *Traffic*. 2:764–774.
47. Inouye, Y., and S. Kawata. 1994. Near-field scanning optical microscope with a metallic probe tip. *Opt. Lett*. 19:159.
48. Renger, J., S. Grafström, …, V. Deckert. 2004. Evanescent wave scattering and local electric field enhancement at ellipsoidal silver particles in the vicinity of a glass surface. *J. Opt. Soc. Am. A Opt. Image Sci. Vis*. 21:1362–1367.
49. Braslavsky, I., R. Amit, …, J. Stavans. 2001. Objective-type dark-field illumination for scattering from microbeads. *Appl. Opt*. 40:5650–5657.
50. He, H., and J. Ren. 2008. A novel evanescent wave scattering imaging method for single gold particle tracking in solution and on cell membrane. *Talanta*. 77:166–171.
51. Born, M., E. Wolf, and A. B. Bhatia. 1980. Principles of Optics. Pergamon, New York.
52. Yasuda, R., H. Noji, …, M. Yoshida. 1998. F_1-ATPase is a highly efficient molecular motor that rotates with discrete 120 degree steps. *Cell*. 93:1117–1124.
53. Shimabukuro, K., R. Yasuda, …, M. Yoshida. 2003. Catalysis and rotation of F_1 motor: cleavage of ATP at the catalytic site occurs in 1 ms before 40 degree substep rotation. *Proc. Natl. Acad. Sci. USA*. 100:14731–14736.
54. Watanabe, R., R. Iino, …, H. Noji. 2008. Temperature-sensitive reaction intermediate of F_1-ATPase. *EMBO Rep*. 9:84–90.
55. Enoki, S., R. Watanabe, …, H. Noji. 2009. Single-molecule study on the temperature-sensitive reaction of F_1-ATPase with a hybrid F_1 carrying a single β(E190D). *J. Biol. Chem*. 284:23169–23176.
56. Sielaff, H., H. Rennekamp, …, W. Junge. 2008. Domain compliance and elastic power transmission in rotary F_0F_1-ATPase. *Proc. Natl. Acad. Sci. USA*. 105:17760–17765.
57. Carter, N. J., and R. A. Cross. 2005. Mechanics of the kinesin step. *Nature*. 435:308–312.
58. Junge, W., O. Pänke, …, S. Engelbrecht. 2001. Inter-subunit rotation and elastic power transmission in F_0F_1-ATPase. *FEBS Lett*. 504: 152–160.
59. Noda, N., and S. Kamimura. 2008. A new microscope optics for laser dark-field illumination applied to high precision two-dimensional measurement of specimen displacement. *Rev. Sci. Instrum*. 79:023704.
60. Rong, G., H. Wang, …, B. M. Reinhard. 2008. Resolving sub-diffraction limit encounters in nanoparticle tracking using live cell plasmon coupling microscopy. *Nano Lett*. 8:3386–3393.
61. Kyriacou, S. V., W. J. Brownlow, and X. H. Xu. 2004. Using nanoparticle optics assay for direct observation of the function of antimicrobial agents in single live bacterial cells. *Biochemistry*. 43:140–147.
62. Lahiri, J., L. Isaacs, …, G. M. Whitesides. 1999. A strategy for the generation of surfaces presenting ligands for studies of binding based on an active ester as a common reactive intermediate: a surface plasmon resonance study. *Anal. Chem*. 71:777–790.